

Article

Study of the Operation of Lead–Acid Battery Electrodes Under Hybrid Battery–Electrolyzer Cycling Profiles

Elisabeth Lemaire , Lionel Serra, Catherine Arnal, Florence Ardiaca, Daniel Monchal, Nicolas Guillet  and Angel Kirchev 

University Grenoble Alpes, CEA, Liten, Campus Ines, 50 Av. de Lac Leman, 73375 Le Bourget du Lac, France; elisabeth.lemaire@cea.fr (E.L.); lionel.serra@cea.fr (L.S.); catherine.arnal@cea.fr (C.A.); florence.ardiaca@cea.fr (F.A.); daniel.monchal@cea.fr (D.M.); nicolas.guillet@cea.fr (N.G.)

* Correspondence: angel.kirchev@cea.fr

Abstract: Flooded lead–acid batteries start producing oxygen and hydrogen during the final stages of charge and subsequent overcharge. The collection of the hydrogen produced allows for an increase in overall energy efficiency and transforms the system into a hybrid device typically referred to as a “Battolyzer” (battery electrolyzer). The present work explores the feasibility of the above approach through a detailed study of the long-term ageing process of flooded tubular lead–acid cells subjected to various rates of discharge and overcharge, emulating four different scenarios of Battolyzer use, starting from 70% depth of discharge cycling to nearly continuous water electrolysis. The combined results from the electrochemical and corrosion studies showed that the Battolyzer cells’ degradation was driven by the corrosion of the positive current collectors. The progress of the corrosion process was strongly correlated with the amount of hydrogen produced. The increase in the depth of discharge resulted in minor decreases in the corrosion current, indicating that the battery functionality of the Battolyzer was more advantageous than the continuous water electrolysis.

Keywords: lead–acid battery; electrolyzer; battery ageing; anodic corrosion; tubular plate



Academic Editor: Adrian Calborean

Received: 29 January 2025

Revised: 14 March 2025

Accepted: 21 March 2025

Published: 31 March 2025

Citation: Lemaire, E.; Serra, L.; Arnal, C.; Ardiaca, F.; Monchal, D.; Guillet, N.; Kirchev, A. Study of the Operation of Lead–Acid Battery Electrodes Under Hybrid Battery–Electrolyzer Cycling Profiles. *Batteries* **2025**, *11*, 137. <https://doi.org/10.3390/batteries11040137>

Copyright: © 2025 by the authors. Licensee MDPI, Basel, Switzerland. This article is an open access article distributed under the terms and conditions of the Creative Commons Attribution (CC BY) license (<https://creativecommons.org/licenses/by/4.0/>).

1. Introduction

The ongoing global decarbonization of sectors like transport and the production of electric power and heat relies strongly on battery and electrochemical electrolyzer technologies for the storage and conversion of electricity from intermittent renewable energy sources. This energy transition process has resulted in an emerging shift in raw material demand from fossil fuels like coal, oil, and natural gas to critical minerals like lithium, cobalt, nickel, copper, rare earths, and precious metals. As a consequence, the development and optimization of electrochemical technologies using noncritical natural resources remain tasks of great importance. Lead is a noncritical natural resource with almost exclusive use in electrochemical applications and, more specifically, lead–acid battery manufacturing. The use of lead outside energy storage applications is continuously declining due to the toxicity of this element. In contrast, in the current state of the art in lead–acid battery manufacturing, use and recycling are considered safe and durable, with collection and recycling efficiency exceeding 99% globally [1]. Lead–acid batteries can be divided into two main categories: “flooded” batteries with free-flowing, liquid sulfuric acid electrolytes and “sealed” or “valve-regulated” batteries with immobilized electrolytes in the form of a thixotropic gel or infused inside an absorptive glass mat (AGM) separator [2]. When the state of charge (SOC) of any lead–acid battery exceeds 70–75%, a

process of oxygen evolution starts at the positive electrode. This oxygen can recombine back into water molecules at the negative electrodes of the valve-regulated cells or it can be vented outside in the case of cells with a “flooded” design. When the SOC of flooded cells exceeds 90–95%, a process of hydrogen evolution starts at the negative electrode. Thus, at the end of the charge and during its overcharge, a flooded lead-acid cell operates as an electrolyzer, producing gaseous hydrogen and oxygen and losing water from the electrolyte. Water electrolysis is considered a “parasitic” process, which decreases the energy efficiency of the battery, causing a need for maintenance (periodic top-up with deionized water) and accelerating the ageing of the positive electrodes through active material shedding and current collector corrosion [3]. The collection of the produced hydrogen can be an opportunity to turn some of the above drawbacks into an advantage. The approach is known in the literature as a battery electrolyzer hybrid cell or simply a “Battolyzer”. Up to now, the concept has mostly been explored by alkaline electrochemical conditions using nickel-based positive electrodes and a variety of negative electrodes [4,5].

The development of a lead-sulfuric acid Battolyzer system is a challenging task due to several particularities of lead electrochemistry. The first one is the poor electrocatalytic properties of lead and lead dioxide electrodes in sulfuric acid solutions, resulting in high hydrogen and oxygen overvoltage and water electrolysis onset above 2.3–2.4 V. The second disadvantage is the durability of the positive electrodes, which is limited by the current collector corrosion and the lead dioxide integrity, which are both accelerated by the process of oxygen evolution [6].

The aim of the present work is to present a detailed study of the lead-acid Battolyzer concept and its feasibility using state-of-the-art “deep-cycling” flooded cells with a tubular positive electrode construction [7]. This offers a combination of confined lead dioxide positive active material (PAM) inside woven or nonwoven textile gauntlets (tubes) and much thicker current collectors. PAM confinement significantly delays the loss of lead dioxide integrity, denoted as “softening and shedding”, while the corrosion of the thicker current collectors takes a longer time. As a consequence, the life cycle of the tubular cells can be very long, from 1000–2000 deep cycles to 6000–7000 full equivalent cycles in a partial state-of-charge mode [8]. According to Pavlov et al., the anodic corrosion process proceeds via a solid-state mechanism of oxygen vacancy insertion into the lead host matrix [9], with kinetics following the Tafel equation [10,11]. The presence of positive active material on the surface of the current collector slows down the corrosion process significantly, while the impact of the polarization mode is more complex [12].

2. Materials and Methods

The experiments were carried out using the flooded tubular cell model “2 HPZS 120”, manufactured by Hoppecke Batteries (Brilon, Germany), using a positive current collector of lead alloy containing 4.2% Sb, 0.09% Sn, and 0.012% Se. Cells with a nominal capacity of 120 Ah and a nominal voltage of 2 V were received in a “dry charged” condition and filled with battery-grade H_2SO_4 electrolyte with a specific gravity of 1.26 $\text{g}\cdot\text{cm}^{-3}$. The ageing tests were carried out on four six-cell strings (12 V/120 Ah battery modules) using Digatron UBT 100-020 ME (Aachen, Germany) battery testing equipment with individual cell voltage monitoring. The experiments were performed at 25 °C in a thermostated water bath with the water level adjusted slightly above the maximum height of the cell electrolyte level, in accordance with aqueous battery testing standards [13]. Prior to the start of the ageing tests, the battery modules were subjected to a “reception test” comprised of 3 cycles with a 10 h rated charge/discharge current (12 A) and 3 more cycles with a 5 h rated current (24 A) in order to estimate the initial capacity and verify the homogeneity of the cell-to-cell performance. The discharge process was terminated by a cut-off voltage value

of 1.75 V per cell. The “IUi” type of charge process was comprised of three steps, starting with a constant current phase (10 h or 5 h rated), followed by a constant voltage stage at 2.4 V per cell and an end of charge step with a constant current of 4 A and a duration of 4.5 h. A measurement of the cell impedance at 1 kHz was performed at the end of this sequence using an HIOKI BT3554 milliohm meter. Four cycling test sequences emulating the hybrid battery–electrolyzer operation under different scenarios are presented in Table 1. They allow the evaluation of the impact of the ratio between the battery and electrolyzer functionalities on the energy efficiency and the electrode degradation mechanism. The cycling was applied during a four-week or eight-week-long period, followed by 3 capacity check-up cycles with 5 h rated current and an overcharge (Tafel) test comprised of constant current staircase increasing from 0 to 20 A. The ageing tests were renewed for another period after the removal of one cell from each battery module. The extracted cells were subjected to supplementary electrochemical tests. They include 3 charge/discharge cycles with 10 h rated current, overcharge test, and impedance spectroscopy tests in two-electrode and three-electrode modes using Ag/Ag₄SO₄/H₂SO₄ reference electrode (+0.65 V vs. SHE). The extracted cells were further subjected to teardown analysis, preceded by an impedance measurement at 1 kHz and electrolyte-specific gravity estimation. The teardown analysis included a visual examination of the cell components, followed by water rinsing and air drying at 60 °C for 48 h of all electrodes. Smaller samples of the extracted negative electrodes were rinsed with ethanol and acetone after the water rinsing in order to prevent the oxidation of the metallic lead from the negative active material during the subsequent drying.

The crystallographic composition of the dried new and aged positive and negative active materials has been characterized with powder X-ray diffraction using a Cu K-alpha ray source.

The corrosion process of the positive current collectors has been studied by the weight loss method [11–13] and by metallographic microscopy observations. Supplementary Information S1 presents a description of the preparation of the samples for the corrosion studies.

Table 1. Battery–electrolyzer hybrid cycling test protocols employing a combination of different depths of discharge (DOD) and charge factor (FC) values.

Test Protocol	DOD (%)	FC (%)	Charge Input (Ah/Cycle)	H ₂ Production (Ah/Cycle)
MOD1: Deep cycling	70	143	120	36
MOD2: Moderate DOD cycling	50	200	120	60
MOD3: Shallow cycling	20	500	120	96
MOD4: Continuous electrolysis	1	10,000	120	118.8

3. Results and Discussion

3.1. Energy Efficiency During the Lead–Acid Cells’ Operation Under Battery–Electrolyzer Cycle Ageing

Energy efficiency is one of the critical parameters for the evaluation of any kind of system for energy conversion and storage. In the case of a battery–electrolyzer hybrid cell, this parameter is more complex and it depends on the way of using the produced hydrogen (as a heat source via burner device or as an electric power source via fuel cell). Since the present research is part of the project Horizon Europe LoCEL-H2 [14], the hydrogen produced during the operation of the lead–acid cells will be considered as a source of heat

for a “clean” cooking process [15]. Thus, a parameter denoted as a “combined energy efficiency” can be defined using the following expression:

$$\eta_E = 100 \frac{E_{\text{discharge}} + \Delta H_{H2}}{E_{\text{charge}}} \quad (1)$$

where $E_{\text{discharge}}$ and E_{charge} are the energies accounted in discharge and charge mode and measured by the battery test equipment, and ΔH_{H2} is the enthalpy of combustion of the produced hydrogen. The latter is calculated as the product between the number of moles of H_2 produced in the overcharge mode (calculated by Faraday’s law) and the specific enthalpy of combustion of the hydrogen ($285.8 \text{ kJ} \cdot \text{mol}^{-1}$ [16]).

Figure 1 presents the cell voltage profiles during the test cycles following the experimental protocols described in Table 1. All four cycling schedules share the same number of Amp-hours applied to the cells in charge mode and different discharge durations corresponding to different values of the depth of discharge (DOD). In this way, we can emulate different scenarios of battery–electrolyzer operation with various shares of hydrogen and electricity demands and a fixed production of electric energy from a renewable source (the latter corresponds to the fixed number of Amp-hours applied during the charge). It should be noted that, in the present work, the parameters DOD and SOC are referenced versus the nominal capacity of the cells according to the following expressions:

$$\text{DOD} = 100 (C_n - Q_{\text{discharge}})/C_n \quad (2a)$$

$$\text{SOC} = 100 - \text{DOD} \quad (2b)$$

where $Q_{\text{discharge}}$ is the number of Amp-hours obtained in discharge mode.

The first profile (also denoted as “MOD1”) shares some similarity with the so-called “battery deep cycling” operation typical for industrial battery applications like forklifts or golf-carts [17]. There are two main differences between the present case and the typical deep cycling. The first one is the use of higher end-of-charge current corresponding to the water electrolysis process. It is equal to $C_n/10h$, where C_n is the nominal capacity of the cell, while, in the “traditional” case, it corresponds to $C_n/20h - C_n/40h$, i.e., two to four times lower. The second different point is the set of a higher charge factor (FC) corresponding to the percentage ratio between the number of Amp-hours in discharge mode and the Amp-hours injected during the subsequent charge ($FC = 100 Q_{\text{charge}}/Q_{\text{discharge}}$). The charge factor is a parameter representing the overcharge applied to the battery cell. The optimal range of the charge factor during the deep cycling of a flooded lead–acid cell is 110–115%, corresponding to 10–15% of overcharge applied, which is necessary for the complete recharge of the cell and the elimination of the electrolyte stratification [17]. In the case of the cycling profile “MOD1”, presented in Figure 1a, the charge factor is equal to 143%, i.e., the applied overcharge is 3–4 times more than usual. The calculation of the combined energy efficiency in this case remains practically constant, close to 75%, almost for the whole duration of the ageing test (9 months corresponding to 584 cycles, without taking into account the periodic check-up tests). This result is in good agreement with the little difference observed between the voltage data.

Figure 1b presents the voltage transients recorded during the tests under the experimental protocol “MOD2”, which combines slightly lower depth of discharge (DOD = 50%) with higher charge factor ($FC = 200\%$), corresponding to more hydrogen produced. The combined energy efficiency under this test profile decreases to 67.5% and does not degrade much despite the excessive overcharge, which is a well-known battery electrode degradation root cause. This lower energy efficiency is related to the high oxygen and hydrogen overvoltage at the positive and negative electrodes of the lead–acid battery [6].

The third battery–electrolyzer operation scenario (denoted also as “MOD3”) is presented in Figure 1c. It starts with a shallow discharge with $DOD = 20\%$ and continues with further increase of the hydrogen production during the overcharge stage. The latter is terminated when the charge factor reaches 500%. The energy efficiency observed during this test mode decreased further down to 57%; however, it also remains rather constant until the end of the tests terminated after 6 months of cycling.

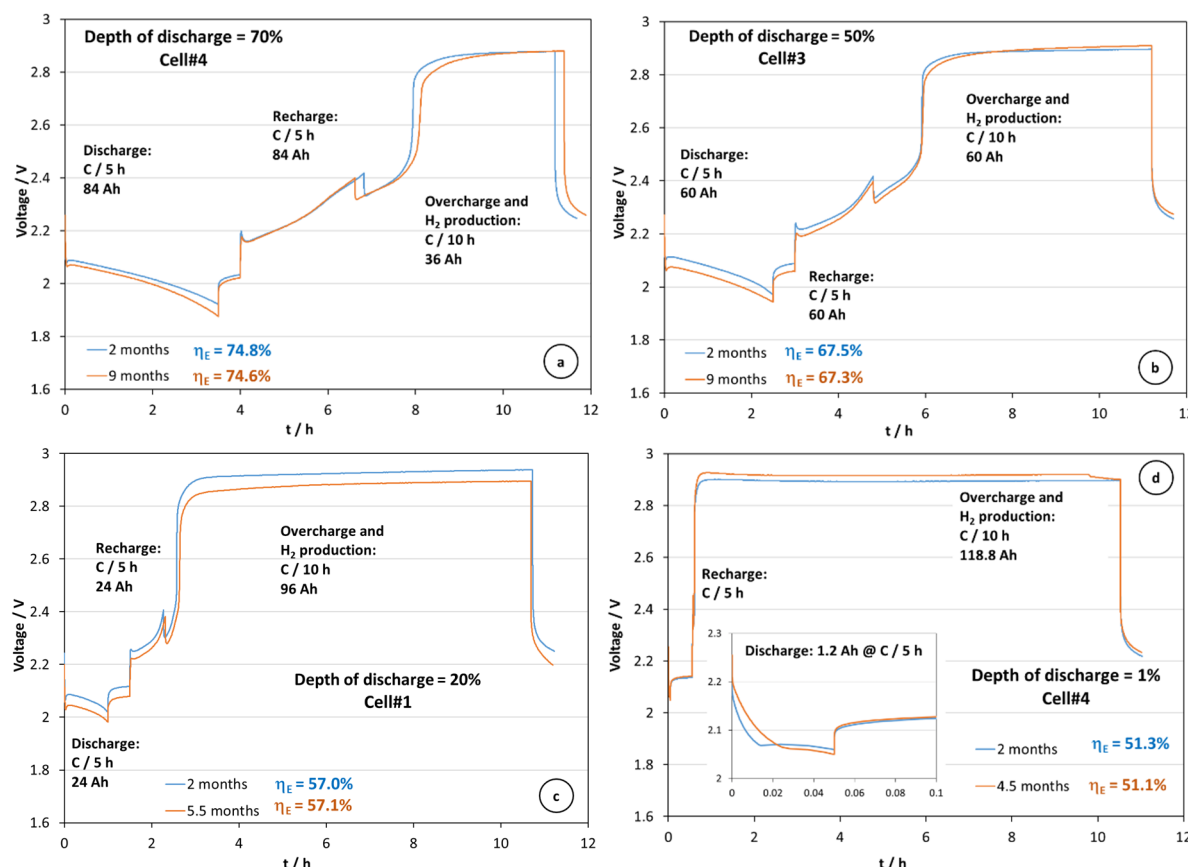


Figure 1. Cell voltage evolution during the test cycling with four battery–electrolyzer operation scenarios (a–d) employing different depths of discharge and extent of overcharge for hydrogen production.

The last cycling mode corresponds to nearly continuous water electrolysis with constant overcharge current equal to $C_n/10h$, interrupted by an hour-long rest period including a short discharge corresponding to $DOD = 1\%$. The combined energy efficiency during this operation scenario is about 51%. It should be noted that the latter exceeds the voltage efficiency considering the theoretical water splitting voltage of 1.23 V and the overcharge voltage plateau of 2.9 V at a current equal to $C_n/10h$. This difference can be explained by the accounting of the hydrogen combustion enthalpy, which sums an entropic and a Gibbs free energy component.

Last but not least, it is important to note that the above-mentioned combined energy efficiency values should be considered as results measured in “ideal” conditions. The latter includes minimum Ohmic resistance of the cells delivered by a very narrow gap between the positive and the negative electrodes, large relative size of the terminals due to the small nominal capacity (the cell model “2 HPZS 120” corresponds to the smallest one in this product range), and a four-point connection scheme excluding the losses due to the cables.

3.2. Electrochemical Kinetics of the Water Electrolysis During the Lead–Acid Cells’ Operation Under Battery–Electrolyzer Cycle Ageing

The operation of the lead–acid cells in hybrid battery–electrolyzer mode and the electrodes’ ageing mechanism were also studied by periodic performance check-up procedures, including capacity measurement and overcharge test. Figure 2 presents a summary of the results of such overcharge tests carried out in single-cell mode right after three capacity estimation cycles, which left the cells completely charged. The overcharge is carried out using an exponential-like, constant-current, staircase profile, presented in Figure 2a. The duration of the overcharge current steps is decreased progressively in order to limit the overall overcharge applied to the cell to 17 Ah or 15% of the nominal capacity and yet to achieve nearly steady-state voltage values. The cell voltage as well as the positive and negative half-cell potentials are further analyzed using semi-logarithmic (Tafel) plots. An Ohmic drop correction was applied to all positive half-cell potential data, knowing that practically all cell degradation phenomena occur at this electrode.

The comparison of data presented in Figure 2b–f shows that all Tafel plots contain two regions—a linear high-current domain corresponding to an overcharge current higher than $\approx C_n/100h$ (1A) and a low-current domain, which does not correlate well with the Tafel equation. The estimated values of the Tafel slope at the negative electrodes remain in the range of 130–160 $\text{mV}\cdot\text{dec}^{-1}$, which is slightly higher than the typical value of 120 $\text{mV}\cdot\text{dec}^{-1}$ [6]. The observed effect of increasing Tafel slopes with the progression of the ageing process can be related to a redistribution of the poorly soluble expander molecules in the porous negative active material. The ageing causes a decrease in the Tafel equation intercept, related to the exchange current density. This effect can be ascribed to the process of transfer of antimony from the corroding positive current collectors to the surface of the negative active material, denoted in the literature as “antimony poisoning” [18]. The main consequence of this process is a decrease in the hydrogen overvoltage, i.e., enhanced hydrogen production. It should be noted that, in the present work, this effect is observed mostly at lower overcharge currents, explaining the small changes of the overcharge voltage plateau observed in Figure 1. The absence of significant antimony poisoning effects (which are much smaller in comparison with the previous experience of our research team) can be related to the “boost charge” effect of the hydrogen production at $C_n/10h$. The latter corresponds to a process of formation of gaseous SbH_3 at the negative electrode, which is readily vented together with the produced hydrogen [18].

The analysis of the Tafel plots of the positive electrodes indicates that the test mode impacts the oxygen evolution kinetics in a different way. The application of cycling profiles with high DOD (Figure 2c,d) results in an increase in the Tafel slope from 70 $\text{mV}\cdot\text{dec}^{-1}$ to 90 $\text{mV}\cdot\text{dec}^{-1}$. The latter corresponds to decreased reversibility of the oxygen evolution, and it can be related to progressive accumulation of PbO_2 with higher crystallinity and lower electrochemical activity [19]. On the other hand, the ageing of the cells under conditions of more intense electrolysis results in a shift in the Tafel lines towards lower overvoltage values without any significant change in the Tafel slope. We can suggest that this effect is due to the increased doping of PbO_2 with Sb(III) and Sb(V) species coming from the accelerated positive grid corrosion, which are causing increased PbO_2 electrochemical activity throughout increased hydration of the PbO_2 particles [20]. It is important to mention that observed oxygen evolution Tafel slopes are fairly close to the typical value of 80 $\text{mV}\cdot\text{dec}^{-1}$ [6].

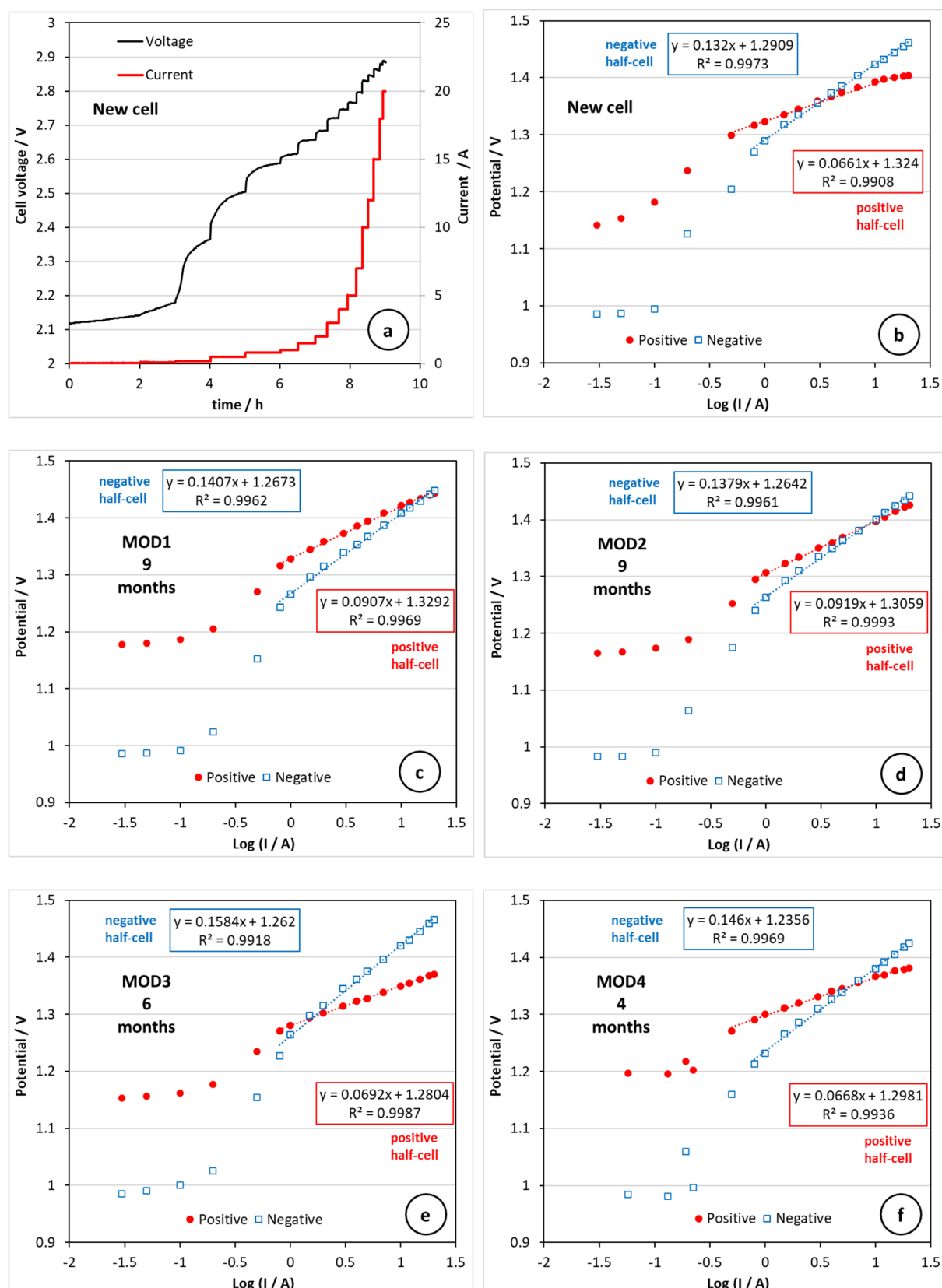


Figure 2. Comparison of the positive and negative half-cell electrochemical kinetics in overcharge mode in the beginning (**a,b**) and at the end of ageing tests with the four battery–electrolyzer operation scenarios (**c–f**). An Ohmic drop correction is applied to the positive half-cell data.

3.3. Evolution of the Discharge Performance Under Battery–Electrolyzer Cycle Ageing Conditions

Figure 3 presents a comparison of the discharge behavior of cells subjected to different periods of ageing using the cycling schedule “MOD4” (“electrolyzer” mode). The discharge tests with a current equal to $C_n/5h$ have been carried out on the entire string, while those with 10 h rated current have been performed in single-cell mode, using a reference electrode for half-cell potential monitoring. Figure 3a presents the discharge performance of Cell#6 from the string 25MOD4. It can be seen that the initial 5 h rated capacity is slightly above 100 Ah, while, with a current equal to $C_n/10h$, this parameter exceeds 120 Ah. The comparison of this result with the data in Figure 3b, presenting the discharge performance of another new cell filled with excess of electrolyte, indicates that the new cells are limited by the positive electrodes, as well as by the electrolyte quantity (the overfilling was due to the absence of a compression jig, which can limit the appearance of a cell wall “dimple”). Figure 3c indicates that, after two months of operation in nearly continuous overcharge mode, the discharge capacity increases above 120 Ah and 140 Ah, respectively, at $C_n/5h$ and $C_n/10h$. The position of both cell voltage transients suggests that there is no significant change in the cell’s internal resistance despite the aggressive overcharge. The analysis of the half-cell potential data shown in Figure 3d indicates that, after the period of 2 months under the profile “MOD4”, the positive electrode is no longer limiting the discharge process and the electrochemical behavior of the cell resembles a battery with a “balanced” ratio between the positive and the negative active material content.

The results presented in Figure 3e show that the cells subjected to 4 months of ageing under the test profile “MOD4” start experiencing a significant loss of discharge performance at 5 h rated current, keeping nearly the same 10 h rated discharge capacity as at the beginning of the tests. The above difference suggests considerable “resistive” ageing [21]. On the other hand, there is no “visible” ageing-related voltage drop increase at the start of the discharge process. The corresponding half-cell potential transients recorded during the $C_n/10h$ discharge test show that the electrochemical behavior is still typical for a battery with a “balanced” ratio between the positive and the negative electrodes. This result is rather unexpected because it is very well known that the ageing mode “MOD4” causes severe and selective degradation of the positive plates.

The data in Figure 3g show that, after five months of operation in electrolyzer mode, the cell lost more than 60% of its nominal capacity at both discharge rates applied. The analysis of the half-cell potential transients in Figure 3h indicates that, at the very end of cell lifetime, the negative electrodes become the capacity-limiting battery component, following the trend observed in Figure 3b,d,f.

Figure 4 presents the evolution of the discharge performance during the check-up cycling of cells from the battery string subjected to the ageing profile “MOD1” (or “deep cycling”), combining a $DOD = 70\%$ and $FC = 143\%$. The discharge performance data corresponding to the beginning of this test are identic with those already discussed above (Figure 3a,b). It can be seen that, in this operation mode, the discharge performance at both currents ($C_n/5h$ and $C_n/10h$) remains nearly constant at the cell and half-cell level, resembling the curves shown in Figure 3c,d.

The comparison between the data in Figures 3 and 4 shows that the impact of the overcharge (i.e., the hydrogen production function of the hypothetical battery–electrolyzer hybrid system) on the cell performance degradation rate is much stronger than the use in battery mode with longer discharge periods. Thus, it is necessary to define a parameter accounting for the overcharge applied to the battery cells, starting from the beginning of their operation.

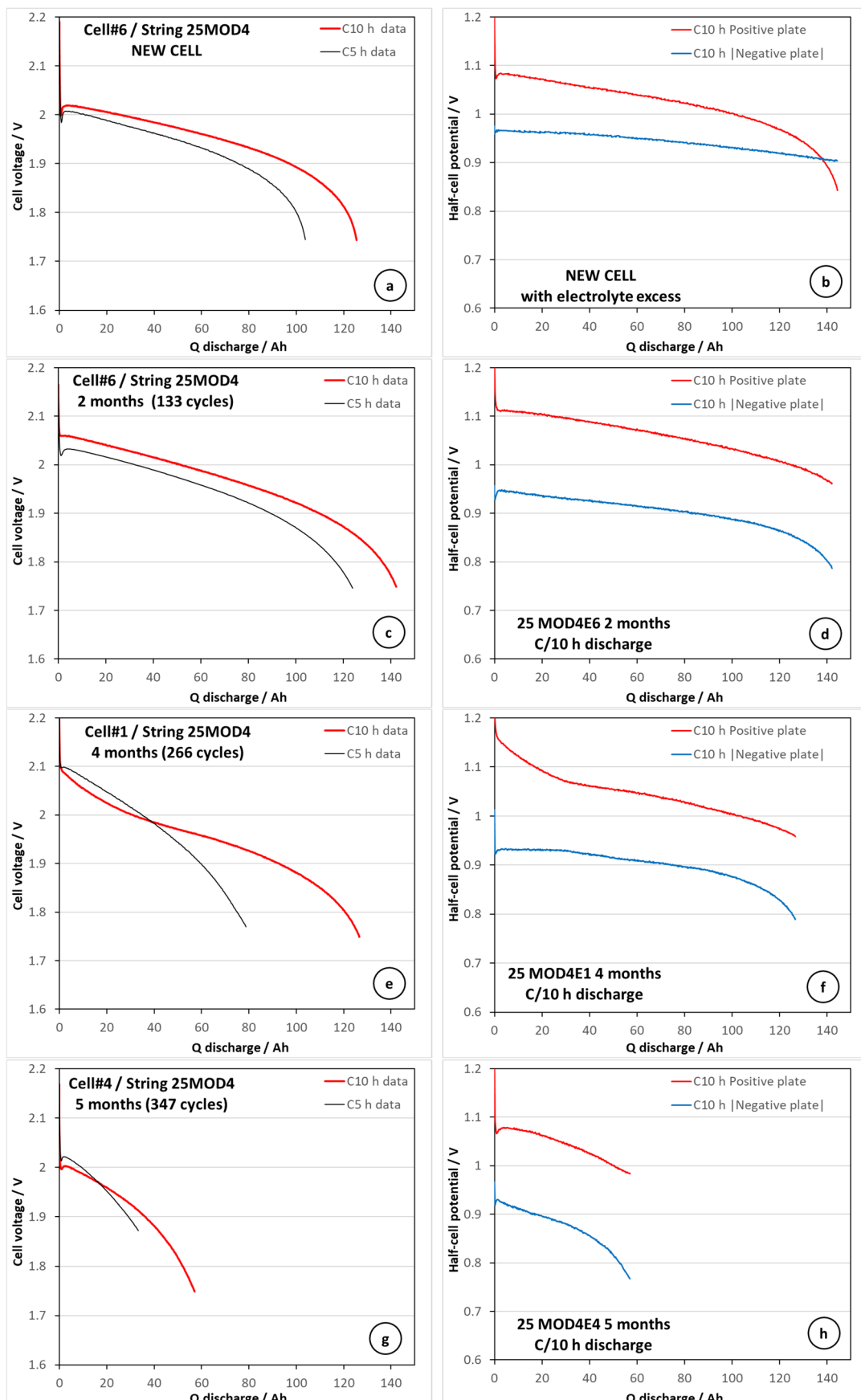


Figure 3. Evolution of the discharge performance of cells cycled under protocol "MOD4/Continuous electrolysis" after 0 (a,b), 2 (c,d), 4 (e,f), and 5 (g,h) months. The negative half-cell potential data are presented with an inverted sign.

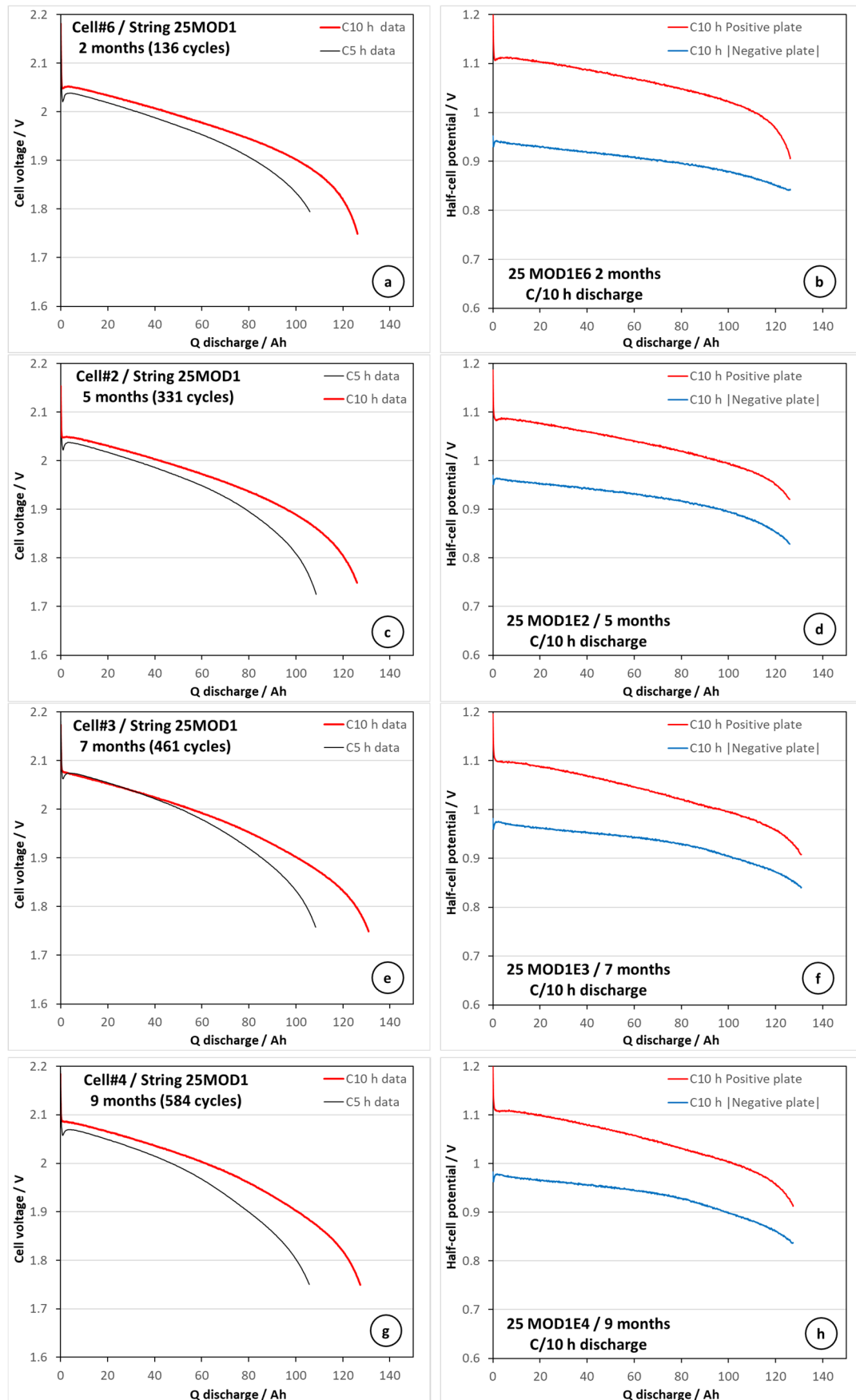


Figure 4. Evolution of the discharge performance of cells cycled under protocol “MOD1/Deep cycling” after 2 (a,b), 5 (c,d), 7 (e,f), and 9 (g,h) months. The negative half-cell potential data are presented with an inverted sign.

Such a parameter can be the cumulative number of Amp-hours overcharge (Q_{ovch}), which is equal to the difference between the cumulative number of Amp-hours in charge/overcharge mode and those in discharge mode:

$$Q_{ovch}(t) = \int_0^t i_{ch}(\tau)d\tau - \int_0^t i_{dsch}(\tau)d\tau \quad (3)$$

where t is the global time of battery cell operation, τ is a local time variable, and $i_{ch}(\tau)$ and $i_{dsch}(\tau)$ represent the charge and the discharge current profiles. If Q_{ovch} is divided by the nominal capacity of the cell C_n , we obtain a dimensionless parameter very similar to the number of equivalent cycles characterizing the battery ageing in partial state of charge applications [21]. Since the overcharge process coincides with the production of hydrogen, we can reference this new parameter as “equivalent cycles of hydrogen production” (H_2 equivalent cycles or n_{H2}).

A summary of the periodic performance check-up tests carried out on all four battery strings is shown in Figure 5. It allows an easier overall assessment of the evolution of discharge performance as a function of the above-defined number of H_2 equivalent cycles. In addition, the DC internal resistance (R_{DC}) at SOC = 100% is also presented. The last parameter is calculated using Ohm’s law, taking into account the applied discharge current and the difference between the open-circuit voltage prior to the start of the discharge and the cell voltage measured after 300 s (U_{300s}) and 600 s (U_{600s}) of discharge:

$$R_{DC} = (OCV - U_{300s})(C_n/5h)^{-1} \quad (4a)$$

$$R_{DC} = (OCV - U_{600s})(C_n/10h)^{-1} \quad (4b)$$

The voltage sampling selection at 300 s and 600 s from the beginning of the discharge corresponds to the point of 1.7% depth of discharge. The latter is positioned on the cell voltage plateau following the “coup de fouet” region related to the nucleation of $PbSO_4$ at the beginning of almost any completely charged lead–acid battery [22]. R_{DC} is a complex parameter with at least two components. Its first component is the Ohmic resistance of the cell, and the second one is the sum of the charge transfer resistance of the discharge reactions at both electrodes.

Figure 5a and 5b show that the lead–acid cell operation under cycling protocol “MOD1” (deep cycling) proceeds with rather small variation in the discharge capacity and an initial decrease in the DC internal resistance to steady-state values. The observed difference between R_{DC} at both discharge rates can be explained by the nonlinear behavior of the charge transfer resistance component, which tends to lower values when the applied current is increased following the Butler–Volmer equation [23]. On the other hand, the initial decrease in R_{DC} can be related to the initial development of a more porous structure of the active materials, which decreases the local current density.

The increase in the hydrogen production share during the operation of the cells under the test protocol “MOD2” results in the appearance of a local minimum and subsequent recovery of the discharge capacity data presented in Figure 5c. A similar kind of irregularity is also observed in the evolution of the R_{DC} shown in Figure 5d. A further increase in the share of overcharge operation during the cycling mode “MOD3” results also in a similar type of “irregular” evolution of the capacity and the internal resistance caused by the joint effect of the active materials cycling and the process of positive current collector corrosion.

The overview of the results from the check-up of the cells subjected to the last test protocol “MOD4” presented in Figure 5g resembles, to a certain extent, the behavior of the lead–acid batteries operating in stand-by mode [24]. On the other hand, the evolution of

the internal resistance values shown in Figure 5h is much slower than expected, no matter that it matches qualitatively the behavior of the discharge capacity presented in Figure 3g.

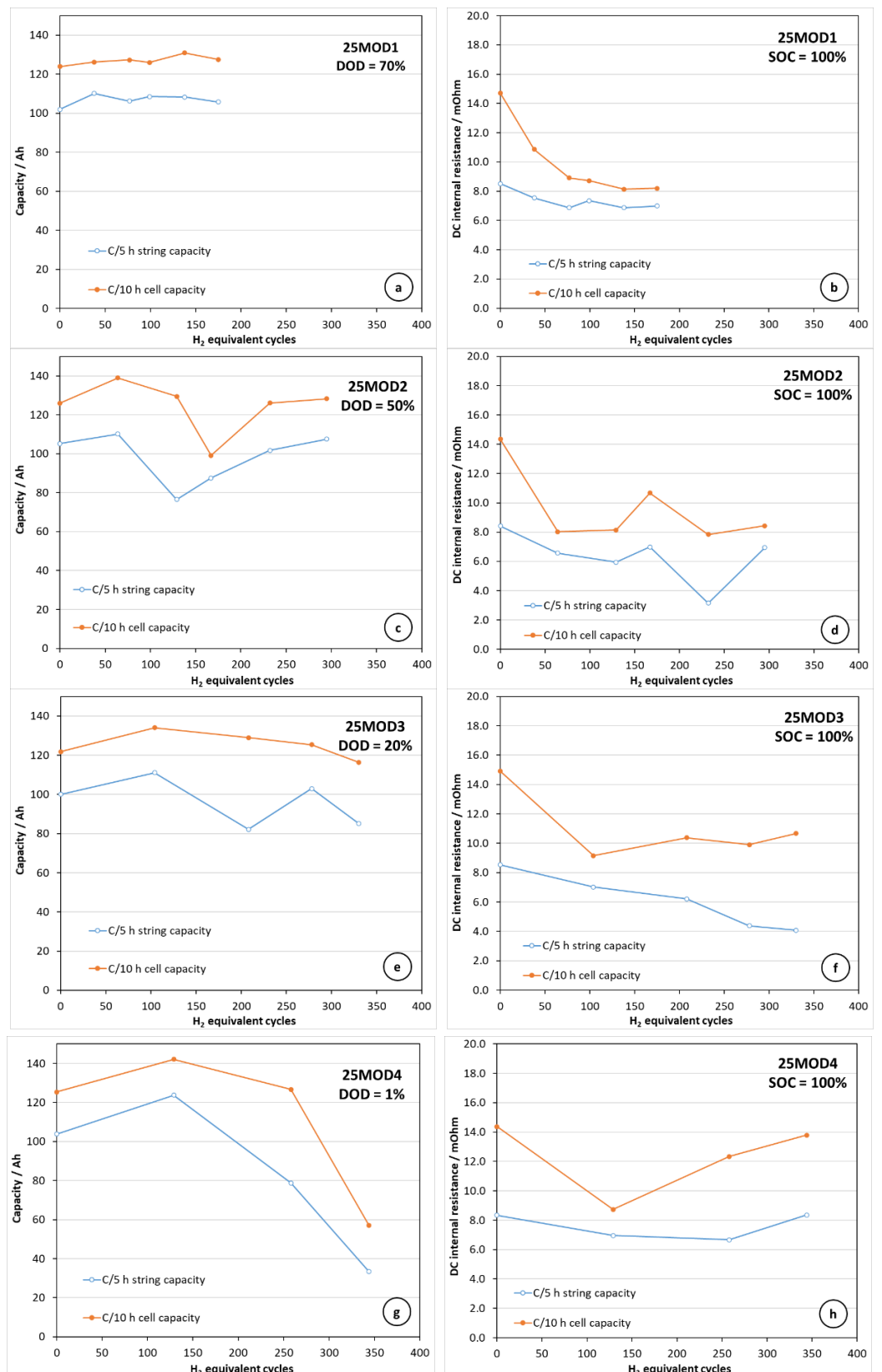


Figure 5. Comparison of the evolution of the discharge capacity (a,c,e,g) and the DC internal resistance at SOH = 100% (b,d,f,h) during the four battery–electrolyzer operation scenarios.

3.4. Evolution of the Electrochemical Impedance During the Battery–Electrolyzer Cycle Ageing

Figure 6 presents the evolution of the electrochemical impedance during the battery–electrolyzer cycle ageing of cells from the strings subjected to the cycling schedules “MOD2” (medium DOD cycling) and “MOD4” (continuous electrolysis mode). The measurements are carried out consecutively in “cell mode” (Figure 6a,b), “positive half-cell mode” (Figure 6c,d), and “negative half-cell mode” (Figure 6e,f) at open circuit, after a 24 h long rest period in an air-conditioned laboratory ($T = 23\text{ }^{\circ}\text{C} \pm 2\text{ }^{\circ}\text{C}$). It was also verified that the sum of the positive and negative half-cell impedance matches the impedance measured directly in cell mode.

The data in Figure 6a,b show that, at the beginning of the ageing under both types of test profiles, there is an initial increase in the cells’ Ohmic resistance (i.e., the spectra shift on the right in the Nyquist plots) without any other significant change in the curves’ pattern. The latter remains very similar to the cases discussed in the literature featuring a high-frequency inductive part related to all metallic pieces in the system (including the cables of the four-point measurement connection to the testing equipment), medium-frequency capacity loop, and low-frequency diffusion (or Warburg) “tail” [25]. The comparison of the different spectra indicates that the gain of the Ohmic resistance is not monotonic and it can feature a local maximum followed by a short decrease before going up again at the stage when the cell capacity starts decaying very fast (the case presented in Figure 6b).

The closer inspection of the positive half-cell impedance spectra presented in Figure 6c,d also indicates an initial increase in the Ohmic resistance related to this electrode and further growth only for the case of the cells from the string subjected to the test protocol “MOD4”. The progression of ageing is also accompanied by the appearance of high/medium-frequency “pseudo-inductive” loop, which can be related to the dynamics of the PbO_2 hydration/dehydration phenomenon and its link with the antimony doping [26].

The analysis of the negative half-cell impedance data indicates that this electrode contributes mostly to the overall cell impedance (it can be seen that the axis of the plots shown in Figure 6a,b,e,f remains the same range, while the positive half-cell impedance is roughly one order of magnitude lower). This particularity is because the specific surface area of the positive active material (porous, nano-sized PbO_2) is about 10 times higher than its counterpart (porous Pb micro-particles) [2]. The data in Figure 6f indicate a significant increase in the negative half-cell impedance, coinciding well with the result presented in Figure 3h (discharge performance limited by the negative electrodes). This rather unexpected result will be further discussed in the next paragraphs, *a priori* knowing that the severe degradation phenomena are concentrated at positive electrodes.

Considering that ageing under the proposed battery–electrolyzer test scenarios impacts mostly the Ohmic resistance of the cells (apart from a relatively short period preceding the practical end-of-life of the positive electrodes), a more detailed analysis of this parameter has been carried out and presented in Figure 7. The plots in Figure 7 contain the Ohmic resistance of the cell (the intercept of the impedance spectrum and the real impedance axis of the Nyquist plot, i.e., Z' values corresponding to $Z'' = 0$), as well as the 1 kHz impedance measured by HIOKI BT3554 apparatus at $SOC = 100\%$ before the launch and after the termination of the ageing tests of the corresponding cell.

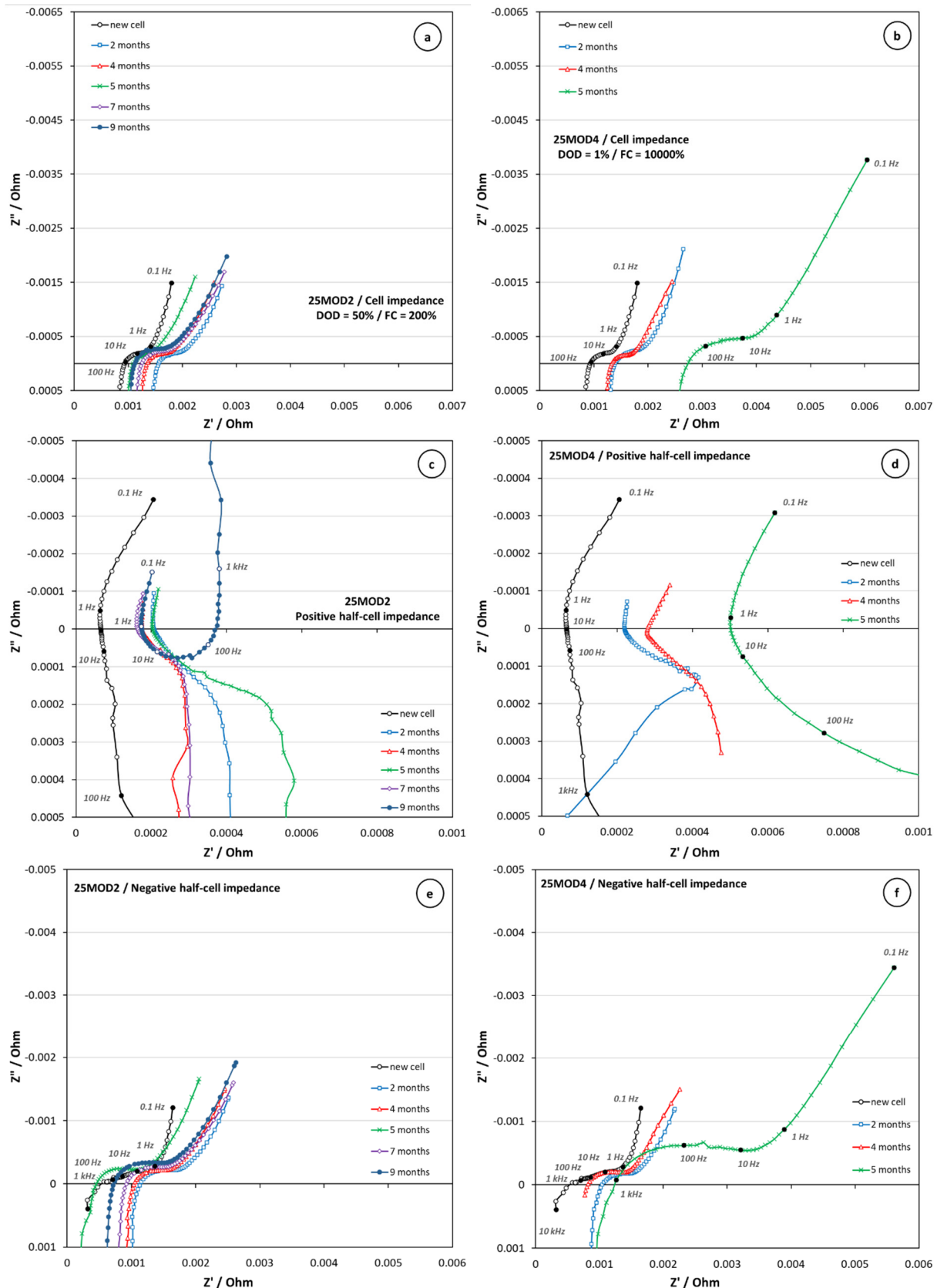


Figure 6. Electrochemical impedance spectra of cells subjected to ageing under the cycling protocols with 50% (a,c,e) and 1% (b,d,f) depth of discharge. The measurements are carried out at open circuit after a 24 h rest period in two-electrode (a,b) and three-electrode mode using a reference electrode (c–f).

The data in Figure 7 show clearly that the Ohmic resistance is very close to the readings of the HIOKI, and both types of data are practically interchangeable. Using this approach, allowing the elimination of the cell-to-cell variations in the Ohmic resistance, one can see the dynamics of the evolution of this parameter. All four studied cases start with a gain in the Ohmic resistance in the range of 0.5 mOhm (with a variation of about $\pm 5\%$). This result can be explained easily with the initial growth of the corrosion layer on the surface of the positive current collectors. The Ohmic resistance passes further a local maximum, corresponding to the above-mentioned gain of 0.5 mOhm. The observed maximum becomes broader under profiles including more intense hydrogen production. The resistance starts increasing again when the end-of-life of the cells approaches (e.g., in Figure 7c,d). The effect observed in Figure 7 is rather unusual for the common lead–acid battery health monitoring practice, but it will be explained using the results from the teardown analysis of the cells presented in the next paragraph.

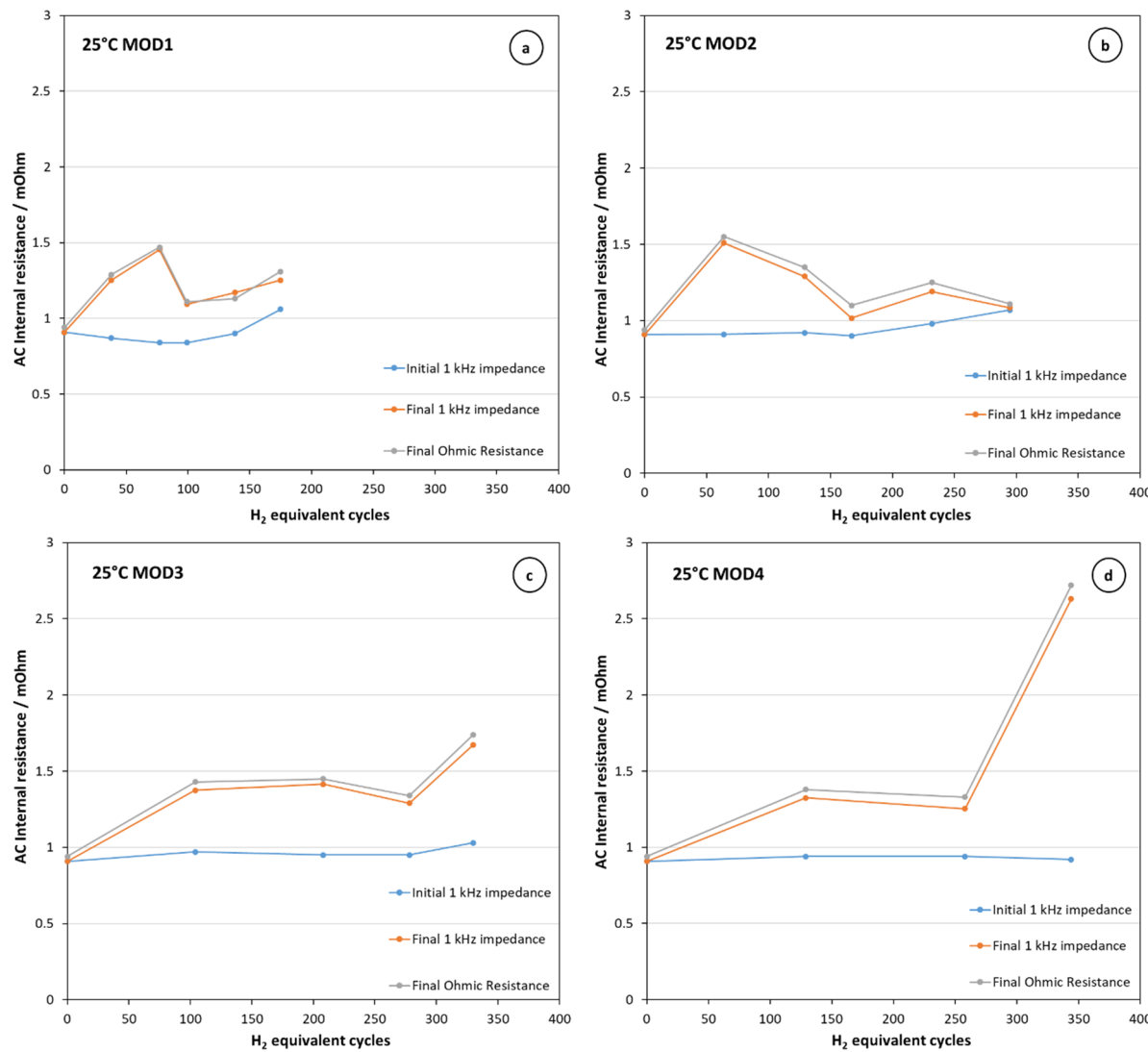


Figure 7. Evolution of the Ohmic resistance, and the AC impedance at 1 kHz, measured on completely charged cells subjected to the four cycling profiles with depth of discharge equal to 70% (a), 50% (b), 20% (c), and 1% (d). The baseline data indicated as “initial 1 kHz impedance” are measured before the launch of the ageing tests, while the rest of the points are measured just before the teardown analysis.

All results of the electric and the electrochemical tests indicate that the dynamics of the ageing processes may remain “hidden” over periods of significant duration. On one

hand, this is an advantage corresponding to a stable operation but, on the other hand, it can be a drawback requiring more sophisticated continuous battery monitoring, including almost mandatory Amp-hour counting in both charge and discharge modes. The latter will permit the practical implementation of the parameter “number of H₂ equivalent cycles” as a precise lead-acid battery or battery-electrolyzer ageing indicator [27].

3.5. Visual Examination of the Cells’ Components and X-Ray Diffraction Characterization of the Active Materials

The study of the mechanisms of operation and degradation of lead-acid battery electrodes under battery-electrolyzer hybrid operational conditions continued with a teardown analysis of the cells subjected to testing with different durations. The first step of this characterization was a visual examination of the completely charged cell’s components. The latter includes the appearance and the texture of the positive and negative electrodes, the state of the positive and negative cast-on-strap welding, as well as the separators. The specific gravity of the electrolyte was measured using a digital hydrometer, together with a visual check for the appearance of an opacity. The results from these tests showed that all visual degradation indicators are concentrated at the positive electrodes. These degradations include swelling, deformations and rupture of the porous gauntlets (appearance of fissures running along the gauntlet length), minor softening of the PbO₂ in the bottom section of the electrodes, and accumulation of very fine PbO₂ particles (referred to as “mud”, which is collected in the so-called “mud-space” on the bottom of the cell casing). There was also a scaling-off of corrosion fragments from the positive current collector sections exposed directly to contact with the electrolyte. The degradation effect of the latter was considered rather marginal due to the considerable thickness of these electrode fragments (about 9–10 mm, in comparison to the current collector spines, which have a diameter of 3 mm). Two cells from the string “MOD3” and two cells from the string “MOD4” failed during the testing due to the appearance of internal short-circuits, which can be associated with the local swelling of some gauntlets, resulting in points of separator squashing. One cell from the string “MOD1” and one cell from the string “MOD2” failed earlier due to a loss of discharge capacity performance. The latter was considered rather as a random anomaly. There was no significant positive current collector height growth at any of the examined cells. The visual effects of the ageing of the electrodes from a cell subjected to five months of ageing under the continuous electrolysis profile “MOD4” can be seen in the Supplementary Information S2.

X-ray diffraction (XRD) was used to evaluate the crystallographic composition of the positive and negative active materials at SOC = 100% using a semi-quantitative phase analysis based on the height of selected diffraction peaks. The positive active materials were prepared from plates washed with tap water until neutral pH, followed by 48 h drying in air at 60 °C. The negative active materials were prepared from disk fragments cut from negative plates washed with tap water until neutral pH. The wet disks were immersed in ethanol for 1 h and, next, in acetone for another hour before putting them to drying in air at 60 °C. The above treatment replaces the water, catalyzing the oxidation of the metallic lead with inert and highly volatile solvents, which are rapidly evaporated from the pores of the samples. Our practice from earlier projects showed that negative active material samples from state-of-the-art new lead-acid batteries contain about 2–3% of tetragonal lead oxide after the above-mentioned washing and drying routine.

The negative active material (NAM) samples from the new cell, subjected to three capacity measurement cycles and a short Tafel test, showed the presence of considerable amounts of orthorhombic and tetragonal lead oxides (o-PbO and tet-PbO) together with the metallic lead, which is the main electrode constituent. One can suggest that the detected lead oxides are an artefact from the dry-charge cell manufacturing process, which remains

even after activation of the cell and initial cycling. At the same time, the data shown in Figure 3b indicate that the detected lead oxide content does not affect the electrochemical performance of the negative plates.

The X-ray diffraction analysis of the NAM samples from the cells analyzed after four months of ageing under the four applied test profiles showed a phase composition similar to that observed for the new cell. After a careful examination of the XRD background signal, it was concluded that there are no detectable traces of PbSO_4 . The XRD analysis of several samples subjected to 5 and 7 months of ageing showed that the amount of o-PbO and tet-PbO decreases progressively. Again, no PbSO_4 was detected.

The positive active material (PAM) sample from the new cell was composed of beta-PbO₂ with minor traces of alpha-PbO₂ (<4% of volume). The PAM samples from cells operated 4 months under the test profiles “MOD1”, “MOD2”, and “MOD3” were found to be composed of more than 99% of the volume of beta-PbO₂. On the other hand, about 4% of alpha-PbO₂ was found in the PAM sample from the cell operated for four months under the profile “MOD4”. It has to be noted that the latter sample was actually a mixture of PAM and a considerable fraction of the thick corrosion layer detached readily from the current collector spines.

PAM samples from the cells cycled during 7 months under the test protocols “MOD1” and “MOD2” were XRD analyzed as well. Again, over 99% of the PAM was composed of beta-PbO₂. The current collector spines from both cells contained a dense and adherent corrosion layer, which was removed after the collection of the main part of PAM by multiple bending of the spines (the corrosion layer fell off the spine surface as scales). The XRD analysis of this mixture of PAM and corrosion layer (there is a significant amount of PAM stuck on the corrosion layer scales) showed the presence of alpha-PbO₂ in volume fractions as high as 45%. This finding is in excellent agreement with the work of Pavlov et al., and it shows that the anodic corrosion process under the hybrid battery–electrolyzer operation modes follows a solid-state mechanism of oxygen species insertion into the lead alloy host matrix [9–12].

All X-ray diffraction data commented on in this paragraph can be found in the Supplementary Information S3–S12.

3.6. Anodic Corrosion of the Positive Current Collectors

The results from the visual examination of the cells’ components and X-ray diffraction characterization of the active materials showed that the corrosion of positive current collector spines is the root cause of the cells’ degradation under hybrid battery–electrolyzer operation scenarios. Figure 8 illustrates the evolution of the corrosion process at cells subjected to the test protocol “MOD4” or nearly continuous water electrolysis. The samples are prepared from the same electrode locations at three levels of the positive plate height. The sampling method is illustrated in the Supplementary Information S1b. The observation of the samples from the new cell subjected to the short initial cycling mentioned previously showed the presence of a relatively thin corrosion layer, with a thickness varying between 15 and 30 μm (the thickness was observed under higher magnification using a metallographic microscope). It can be seen that, after 2 months of ageing, the thickness of the corrosion layer increases to 0.7–0.9 mm. The latter values are doubled after another 2 months of ageing. It should be mentioned that, after 5 months of ageing under the same test protocol, the remaining fragments of the current collector spines were too small, and it was not possible to prepare samples for microscopy observations. The comparison of the micrographs corresponding to the different positive plate heights shows that the corrosion process remains rather homogeneous during the majority of the cells’ lifetime. Taking into account the discharge performance data in Figure 3g, it can be suggested that, after

4 months of ageing, the spine diameter is close to the critical threshold. The micrographs corresponding to 4 months of testing also indicate that, beyond this point, the corrosion mechanism changes from a homogeneous process towards “pitting”, which may cut the current collector spines horizontally.

The quantitative estimation of the corrosion rate was based on the measurement of the surface area of the metallic part of the spine’s cross-section, instead of using the corrosion layer thickness, which may vary or even be transformed into more porous PbO_2 active material (especially under the other test profiles employing high depth of discharge). The measurement was based on the estimation of four characteristic diameters (long, short, and two diagonals) and the use of the mean diameter to calculate the surface of the perpendicular cross-section of a cylindrical wire.

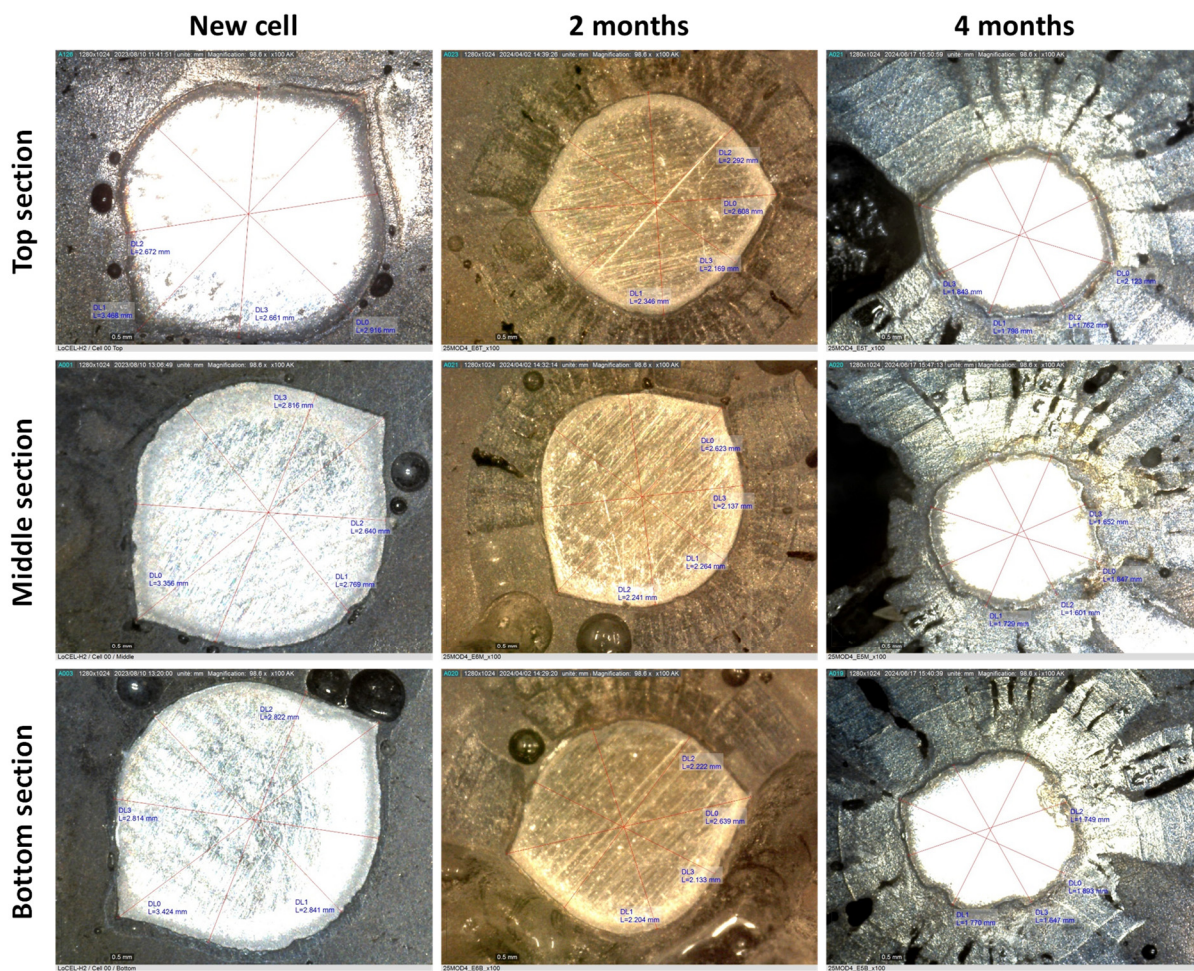


Figure 8. Digital micrographs of current collector spine cross-sections extracted from cells aged under the cycling protocol with a depth of discharge equal to 1% (MOD4).

The resulting change in the spine diameter was converted into a volume loss of metallic lead per centimeter of spine length and, next, into a weight loss per square centimeter of initial spine area (using $\text{mg} \cdot \text{cm}^{-2}$ units) by simplifying the alloy composition to pure lead.

The summary of the current collector weight loss measurements based on the microscopy observations is shown in Figure 9. The corrosion data from all four test profiles can be compared by using the quantity of the produced hydrogen (the applied overcharge) as the x-axis. It can be seen that there is a nearly linear correlation between the weight loss and the number of H_2 equivalent cycles. The results also indicate that the test mode exerts rather a small impact on the corrosion rate. The data also show that the corrosion is slightly faster in the bottom section of the electrodes and slightly lower in the middle

section. The mechanism behind this minor spatial distribution of the corrosion process is complex. It is hard to relate it to the electrolyte stratification, for example, especially in the case of the data in Figure 9d, due to the negligible share of the discharge process and the constant gassing. The observation of slightly faster corrosion in the bottom and the top section of the electrode is also in good agreement with the work of Guo et al., describing a local increase in the tubular electrode's resistance in their top and bottom sections [28].

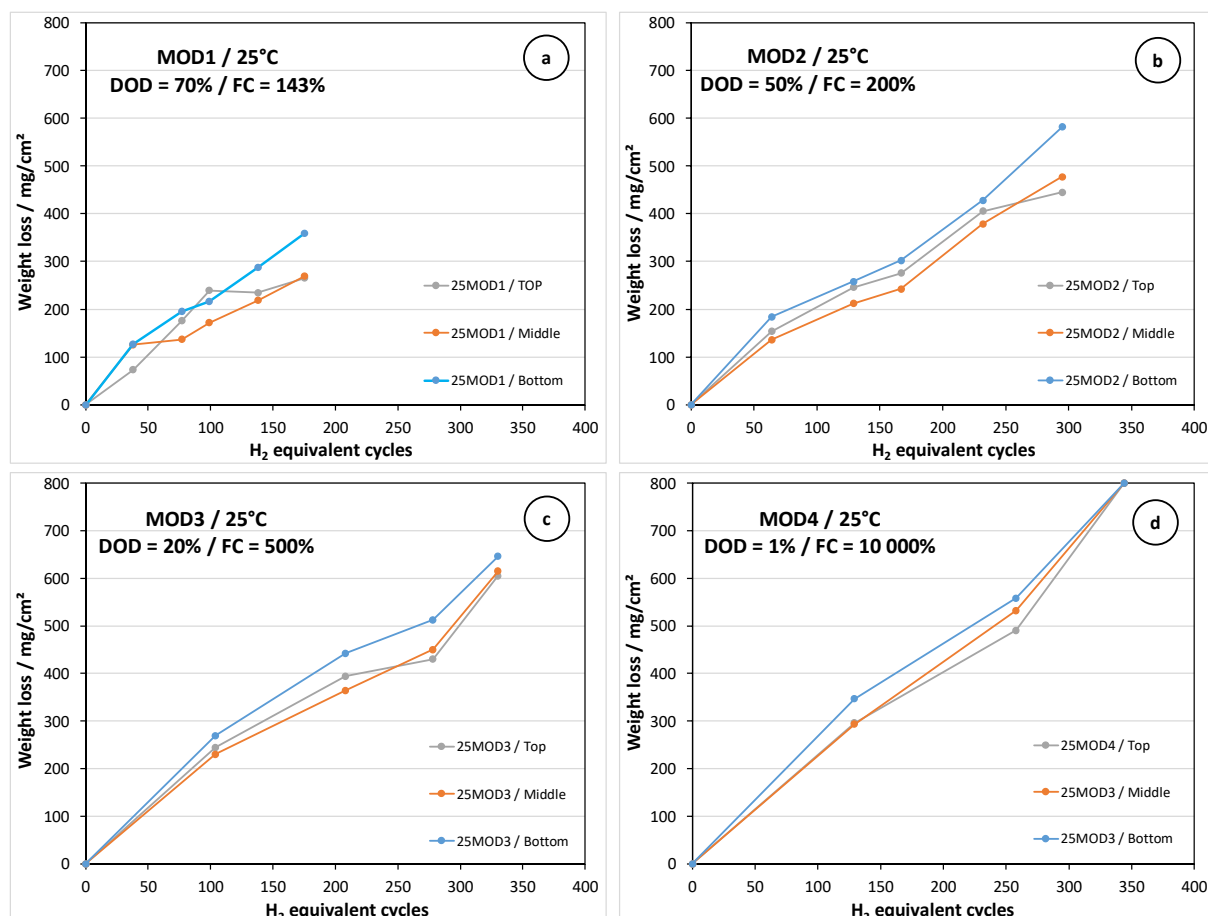
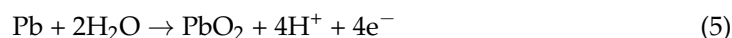


Figure 9. Summary of the corrosion rate measurements estimated by digital microscopy observations of samples from cells aged under the battery–electrolyzer operation scenarios “MOD1” (a), “MOD2” (b), “MOD3” (c), and “MOD4” (d).

Figure 10 presents the results from the corrosion rate measurements using the weight loss method. The estimation is carried out using four positive current collector spines cut to a length of 223 mm ± 1 mm. The results shown in Figure 10a are very similar to the data plotted in Figure 9. It can be seen that the corrosion process under the test profile “MOD4” is slightly faster than the other three cases. The measurements presented in Figure 10a have been used to estimate the partial current corresponding to the electrochemical process of corrosion defined with the reaction:



The application of Faraday’s law for the above reaction can be expressed as:

$$i_{corr} = \frac{4\Delta m_{spine}F}{\Delta t_{electrolysis}A_{Pb}} \quad (6)$$

where i_{corr} is the corrosion current, Δm_{spine} is the current collector weight loss, F is Faraday's constant, $\Delta t_{electrolysis}$ is the duration of the H_2O electrolysis, and A_{Pb} is the atomic weight of the lead. The term $\Delta t_{electrolysis}$ is calculated as the ratio between the number of amp-hours of overcharge and the applied overcharge current, equal to $C_n/10h$.

Figure 10b shows that the corrosion current remains close to $0.1 \text{ mA} \cdot \text{cm}^{-2}$. This result allows modeling of the corrosion process as independent of the depth of discharge. However, it is expected to vary strongly with the change in the temperature and the water electrolysis current (which, in its turn, defines the electrode potential following the Tafel plots shown in Figure 2b–f) [10–12].

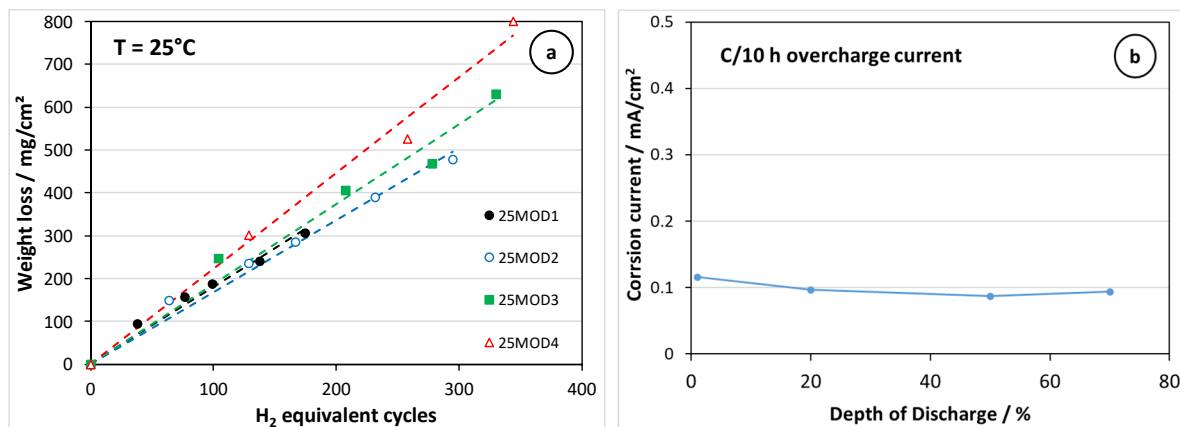


Figure 10. Summary of the corrosion rate measurements estimated by the weight loss method (a) and the corresponding values of the corrosion current as a function of the depth of discharge (b).

3.7. Evolution of the Positive Electrode Deformation During the Ageing Process

The process of positive electrode “growth” is an important and very adverse effect caused by the positive current collector corrosion [24]. It is driven by the difference between the density of the lead ($11.35 \text{ g} \cdot \text{cm}^{-3}$ or $54.8 \text{ mmol} \cdot \text{cm}^{-3}$) and that of the lead dioxide ($9.4 \text{ g} \cdot \text{cm}^{-3}$ or $39.3 \text{ mmol} \cdot \text{cm}^{-3}$). The tubular plate construction allows rather clear tracking down of this process using microscopy observations, such as the ones presented in Figure 11 for the case of the cycling profile “MOD4”. In the present work, the term “thickness” coincides fairly well with the internal diameter of the gauntlet, which was measured once directly and twice using a three-point circle fitting function of the digital microscope software. The results from these measurements can be further transformed into strain (or deformation) using the samples from the new cell as a reference. The evolution of the gauntlet strain (corresponding also to the electrode thickness growth) is summarized in Figure 12. Starting “back-forward” from the case corresponding to the profile with $DOD = 1\%$, shown in Figure 12d, one can see that the corrosion process causes progressive thickness growth, which is more significant in the middle and bottom sections of the positive electrode. The data indicate that there is a critical strain threshold of the gauntlets, being in the range of 11–12%. The increase in the electrode thickness beyond this point results in gauntlet tissue rupture running along the seams. The result from this observation is marked as a dotted asymptote sketching a rapid increase in the strain (Figure 12c,d).

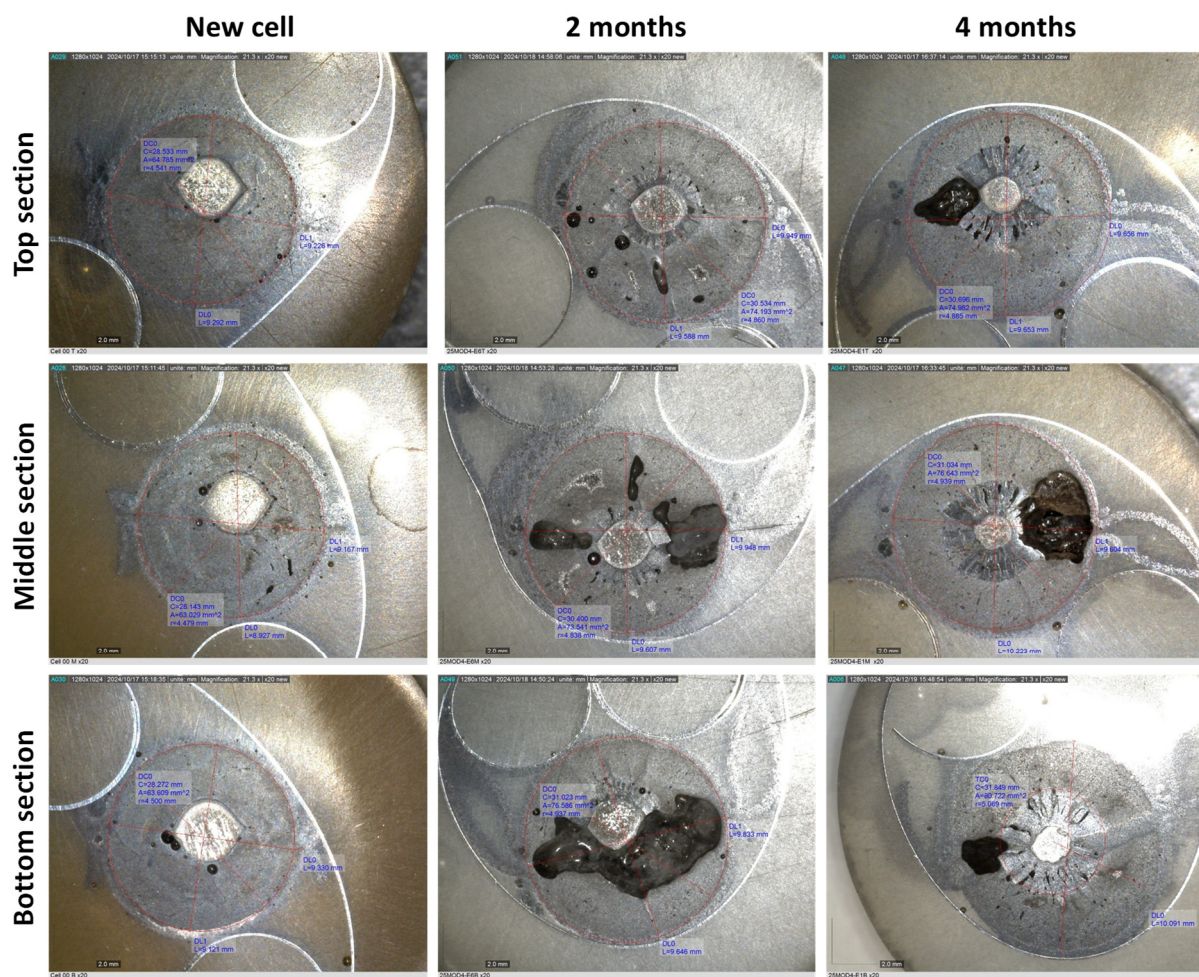


Figure 11. Digital micrographs of the whole gauntlet cross-sections of tubular electrodes extracted from cells aged under the cycling protocol with a depth of discharge equal to 1% (MOD4).

The evolution of the gauntlet deformation becomes more complex with the increase in the depth of discharge. This complexity can be related to the cyclic change in the electrodes' thickness due to the periodic formation and depletion of PbSO_4 , which is less dense ($6.29 \text{ g}\cdot\text{cm}^{-3}$ or $20.8 \text{ mmol}\cdot\text{cm}^{-3}$) than PbO_2 . The latter phenomenon is “balanced” by the tensile strength and the elasticity of the gauntlet material, which applies a sort of “dynamic” compression, preventing (or at least delaying) the occurrence of PAM softening and shedding [29,30]. As a result of this “balance”, one can see even a gauntlet shrinkage phenomenon (negative strain) located in the top section of the electrodes. The increase in the DOD to 70% results in homogenization of the strain distribution along the electrode height. Despite the observed variations, it is clear that the electrode thickness increases due to the corrosion process, resulting in a decreased gap between the positive and negative plates. The latter explains fairly the observed variations in the ohmic resistance of the cells along the ageing (Figure 7a–c). Last, but not least, it should be mentioned that the massive gauntlets rupture matches rather well the moment of discharge performance failure related to current collector spine ultimate corrosion damage.

The data in Figure 12 show clearly that the hybrid type of operation, combining higher DOD values and a smaller share of hydrogen production, will be much more beneficial in terms of cells' lifetime in comparison with the regimes of continuous water electrolysis. Apart from this, the positive electrode's durability can be improved by using alloys with higher corrosion resistance [2,3,6], tubular plates with thicker spines, as well as woven gauntlets with superior mechanical performance [29].

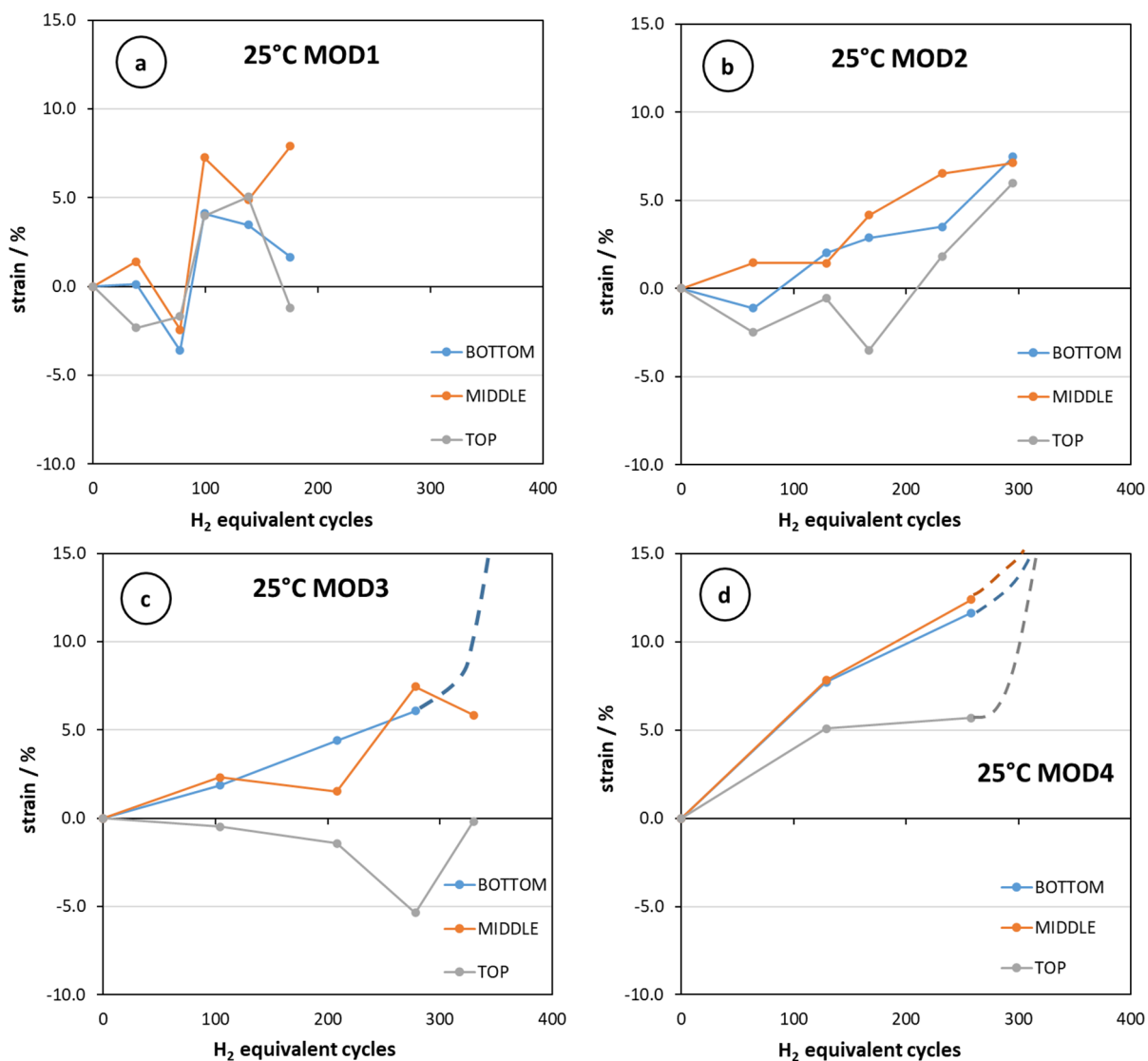


Figure 12. Evolution of the tubular electrode gauntlet strain during the cycling of cells under battery–electrolyzer operation scenarios with depth of discharge equal to 70% (a), 50% (b), 20% (c), and 1% (d).

4. Conclusions

The operation of the flooded traction lead–acid battery cells with tubular positive electrodes has been studied under test protocols combining charge/discharge operation and excessive overcharge corresponding to the use of the cells in water electrolyzer mode. The whole ensemble of the results obtained under four operation scenarios showed that the lead-based battery–electrolyzer hybrid electrochemical system could be an interesting candidate for a variety of renewable energy conversion and storage applications. The latter includes emergent use cases like long-duration energy storage and opportunity purchase of cheap (or even negative-priced) electricity and its conversion into much more pricy hydrogen.

The electrochemical and electric tests showed that the efficiency of the hybrid operation increases with the increased share of the “battery function”, as it might exceed 75% under profiles combining deep cycling and intense overcharge. The monitoring of the cells’ operation indicated that the ageing process in battery–electrolyzer modes proceeds without any significant degradation of the electric performance over significant periods, covering

more than 80% of the total cell lifetime. This feature makes the use of Amp-hour counting (battery history bookkeeping) a critical part of the battery–electrolyzer monitoring.

The teardown analysis of the cells subjected to hybrid cycling profiles showed that the positive grid corrosion is the main degradation mechanism, while the negative electrodes remain practically intact. The corrosion process evolution follows closely the quantity of the applied total overcharge (i.e., the quantity of the produced H₂). The increase in the depth of discharge (i.e., the “battery function”) results in a minor decrease in the corrosion rate, indicating that the hybrid lead-based battery–electrolyzer cells’ use with H₂ production as a “by-product” can be profitable, especially in emerging applications of renewable energy storage and conversion.

Supplementary Materials: The following supporting information can be downloaded at: <https://www.mdpi.com/article/10.3390/batteries11040137/s1>, Figure S1a: Digital image of washed and dried positive tubular electrode from a new cell; Figure S1b: Digital image of an entire gauntlet prepared for cutting, in order to get samples for optical metallographic observations.; Figure S2: Images of negative (left) and positive (right) electrodes extracted from new cell and from a cell operated as part of the string 25MOD4 during 5 months.; Figure S3: X-diffraction patterns of negative active materials from cells underwent 0, 4 and 5 months of aging at cycling protocol 25MOD1; Figure S4: X-diffraction patterns of negative active materials from the cell underwent 5 months of aging at cycling protocol 25MOD1; Figure S5: X-diffraction patterns of positive active materials from cells underwent 0, 4 and 5 months of aging at cycling protocol 25MOD1; Figure S6: X-diffraction patterns of negative active materials from cells underwent 4, 5 and 7 months of aging at cycling protocol 25MOD2; Figure S7: X-diffraction patterns of negative active materials from the cell underwent 7 months of aging at cycling protocol 25MOD2; Figure S8: X-diffraction patterns of positive active materials from cells underwent 4, 5 and 7 months of aging at cycling protocol 25MOD2; Figure S9: X-diffraction patterns of negative active material from a cell underwent 4 months of aging at cycling protocol 25MOD3. Figure S10: X-diffraction patterns of positive active material from a cell underwent 4 months of aging at cycling protocol 25MOD3; Figure S11. X-diffraction patterns of negative active material from a cell underwent 4 months of aging at cycling protocol 25MOD4; Figure S12. X-diffraction patterns of positive active material from a cell underwent 4 months of aging at cycling protocol 25MOD4.

Author Contributions: Conceptualization, E.L. and A.K.; methodology, A.K.; validation, N.G.; formal analysis, A.K., E.L. and N.G.; investigation, N.G.; data curation and technical support, C.A., F.A., D.M. and L.S.; writing—original draft preparation, A.K.; writing—review and editing, E.L. and N.G.; visualization, A.K. All authors have contributed substantially to the work reported. All authors have read and agreed to the published version of the manuscript.

Funding: This work has been realized in association with INES.2S within the French national program Investments for the Future (ANR-10-IEED-0014-01) and received funding from the European Union’s Horizon Europe research and innovation program under the grant “Low-Cost, Circular, plug & play, off grid Energy for Remote Locations including Hydrogen” (Project LoCEL-H2-101096033).

Data Availability Statement: The data presented in Figures 1–12 are available for download at the Horizon Europe LoCEL-H2 project website: <https://locelh2.org/> (accessed on 1 June 2024).

Acknowledgments: AK would like to thank Dani Strickland, Eduardo Cattaneo, and Goetz Langer for the helpful discussions of the tests design and the obtained results.

Conflicts of Interest: The authors declare no conflicts of interest. The funders had no role in the design of the study; in the collection, analyses, or interpretation of data; in the writing of the manuscript; or in the decision to publish the results.

Abbreviations

The following abbreviations are used in this manuscript:

DOD	Depth of Discharge
SOC	State of Charge
PAM	Positive Active Material
NAM	Negative Active Material
FC	Charge Factor
XRD	X-ray diffraction

References

1. Vault Consulting. *National Recycling Rate Study (Study Years 2017–2021)*, Battery Council International, Chicago. 2023. Available online: <https://battery council.org/resource/national-recycling-rate-study/> (accessed on 29 January 2025).
2. Pavlov, D. *Lead-Acid Batteries: Science and Technology*, 2nd ed.; Elsevier: Amsterdam, The Netherlands, 2017.
3. Ruetschi, P. Aging mechanisms and service life of lead-acid batteries. *J. Power Sources* **2004**, *127*, 33. [[CrossRef](#)]
4. Mulder, F.M.; Weninger, B.M.H.; Middelkoop, J.; Ooms, F.G.B.; Schreuders, H. Efficient electricity storage with a battolyser, an integrated Ni-Fe battery and electrolyzer. *Energy Environ. Sci.* **2017**, *10*, 756.
5. Barton, J.P.; Gammon, R.J.L.; Rahil, A. Characterisation of a Nickel-iron Battolyser, an Integrated Battery and Electrolyser. *Front. Energy Res.* **2020**, *8*, 509052.
6. Berndt, D. *Maintenance-Free Batteries Based on Aqueous Electrolyte Lead-Acid, Nickel/Cadmium, Nickel/Metal Hydride: A Handbook of Battery Technology*, 3rd ed.; Research Studies Press: Boston, MA, USA, 2003.
7. Rogatchev, T.; Papazov, G.; Pavlov, D. The effect of current density and thickness of the active mass upon the corrosion rate of the spines of lead-acid battery plates. *J. Power Sources* **1983**, *10*, 291.
8. Wagner, R. Large lead/acid batteries for frequency regulation, load levelling and solar power applications. *J. Power Sources* **1997**, *67*, 163. [[CrossRef](#)]
9. Pavlov, D. Processes in solid state at anodic oxidation of a lead electrode in H_2SO_4 solution and their dependence on the oxide structure and properties. *Electrochim. Acta* **1978**, *23*, 845. [[CrossRef](#)]
10. Rogatchev, T.; Ruevski, S.; Pavlov, D. Mechanical and corrosion properties of low antimony lead alloys. *J. Appl. Electrochem.* **1976**, *6*, 33. [[CrossRef](#)]
11. Pavlov, D.; Rogachev, T. Dependence of the phase composition of the anodic layer on oxygen evolution and anodic corrosion of lead electrode in lead dioxide potential region. *Electrochim. Acta* **1978**, *23*, 1237. [[CrossRef](#)]
12. Papazov, G.; Rogatchev, T.; Pavlov, D.; Garche, J.; Wiesener, K. Influence of the lead dioxide active mass on the corrosion rate of the spines of positive lead-acid battery plates. *J. Power Sources* **1981**, *6*, 15.
13. Hildebrandt, T.; Osada, A.; Peng, S.; Moyer, T.J. Chapter 19—Standards and Tests for Lead-Acid Batteries in Automotive Applications. In *Lead-Acid Batteries for Future Automobiles*; Garche, J., Karden, E., Moseley, P.T., Rand, D.A.J., Eds.; Elsevier: Amsterdam, The Netherlands, 2017.
14. Horizon Europe LoCEL-H2 Project Web Site. Available online: <https://locelh2.org/> (accessed on 29 January 2025).
15. Hutton, T.; Hammond, J.; Roberts, D.; Barton, J.; Wilson, J.; Strickland, D.; Brown, S. Lead-acid battolysers for hydrogen cooking: A comparison with electric cooking for sub-Saharan Africa. *Energy Sustain. Dev.* **2024**, *81*, 101491.
16. Haynes, W.M. *CRC Handbook of Chemistry and Physics*; CRC Press: Boca Raton, FL, USA, 2014.
17. Pavlov, D. Chapter 5.1 Lead-Acid Batteries. In *Power Sources for Electric Vehicles*; McNicol, B.D., Rand, D.A.J., Eds.; Elsevier Sequoia: Amsterdam, The Netherlands, 1984; p. 421.
18. Boehnstedt, W.; Radel, C.; Scholten, F. Antimony poisoning in lead-acid batteries. *J. Power Sources* **1987**, *19*, 301. [[CrossRef](#)]
19. Pavlov, D. The Lead-Acid Battery Lead Dioxide Active Mass: A Gel-Crystal System with Proton and Electron Conductivity. *J. Electrochem. Soc.* **1992**, *139*, 3075. [[CrossRef](#)]
20. Monahov, B.; Pavlov, D. Influence of Antimony on the Structure and the Degree of Hydration of the Anodic PbO₂ Layer Formed on Pb-Sb Electrodes. *J. Electrochem. Soc.* **1994**, *141*, 2316. [[CrossRef](#)]
21. Kirchev, A. Chapter 20—Battery Management and Battery Diagnostics. In *Electrochemical Energy Storage for Renewable Sources and Grid Balancing*; Moseley, P.T., Garche, J., Eds.; Elsevier: Amsterdam, The Netherlands, 2015.
22. Delaille, A.; Perrin, M.; Huet, F.; Hernout, L. Study of the coup de fouet of lead-acid cells as a function of their state-of-charge and state-of-health. *J. Power Sources* **2006**, *158*, 1019.
23. Karden, E. Using Low Frequency Impedance Spectroscopy for Characterization, Monitoring, and Modeling of Industrial Batteries. PhD Thesis, Shaker, Aachen, Germany, 2002.
24. Giess, H. The influence of calcium, tin and grid thickness on corrosion-induced grid growth. *J. Power Sources* **1995**, *53*, 31.

25. Keddam, M.; Stoynov, Z.; Takenouti, H. Impedance measurement on Pb/H₂SO₄ batteries. *J. Appl. Electrochem.* **1977**, *7*, 539. [[CrossRef](#)]
26. Kirchev, A.; Delaille, A.; Perrin, M.; Lemaire, E.; Mattera, F. Studies of the pulse charge of lead-acid batteries for PV applications. Part II. Impedance of the positive plate revisited. *J. Power Sources* **2007**, *170*, 495.
27. Kirchev, A.; Guillet, N.; Serra, L. Method for Diagnosing and Predicting Service Life of Lead Acid Batteries, in Particular for Storing Backup Energy. European Patent EP4198538 (A1), 21 June 2023.
28. Guo, Y.; Li, W.; Zhao, L. A study of current and potential distributions on tubular positive plate. *J. Power Sources* **2003**, *116*, 193.
29. Terzaghi, G. Engineered woven gauntlets to improve the performance of lead/acid tubular plates. *J. Power Sources* **1998**, *73*, 78.
30. Ferreira, A.L. Positive-plate gauntlets—The non-woven fabric solution. *J. Power Sources* **1998**, *73*, 86.

Disclaimer/Publisher’s Note: The statements, opinions and data contained in all publications are solely those of the individual author(s) and contributor(s) and not of MDPI and/or the editor(s). MDPI and/or the editor(s) disclaim responsibility for any injury to people or property resulting from any ideas, methods, instructions or products referred to in the content.